NUMERICAL PREDICTIONS OF DUST-INDUCED HEAT FLUX AUGMENTATION IN HYPERSONIC BLUNT-BODY FLOWS USING A DISCONTINUOUS GALERKIN MULTIPHASE FLOW SOLVER

Eric J. Ching
Stanford University
Stanford, CA 94305, USA

Michael D. Barnhardt
NASA Ames Research Center
Moffett Field, CA 94035, USA

Matthias Ihme
Stanford University
Stanford, CA 94305, USA

ABSTRACT

Recent interest in human-scale missions to Mars has motivated the need for high-fidelity simulations of reentry flows. During a dust storm, there can be high levels of suspended dust in the Martian atmosphere, which can not only enhance erosion of thermal protection systems but also transfer energy and momentum to the shock layer, thereby significantly augmenting the surface heat flux. Second-order finite-volume schemes are typically employed for hypersonic flow simulations, but such schemes suffer from a number of disadvantages. An attractive alternative is discontinuous Galerkin methods, which benefit from arbitrarily high spatial order of accuracy, geometric flexibility, and other properties. To enable accurate computations of high-speed particle-laden flows, an Euler-Lagrange methodology was developed in which the Eulerian field of the carrier gas is calculated using a discontinuous Galerkin scheme while the disperse phase is treated with Lagrangian particle tracking. We discuss challenges associated with coupling these two formulations and how to handle them. Momentum and energy transfer between the carrier gas and the particle phase is considered, and the importance of accounting for interparticle collisions is assessed. In addition, we describe the physical model of the particle phase and examine effects of its uncertainties on the numerical solution. We demonstrate the performance of the Euler-Lagrange method in representative test cases, with focus on the accurate prediction of particle trajectories and heating augmentation. Quantitative comparisons with experiments are provided.

Index Terms— Discontinuous Galerkin method, Lagrangian particle tracking, Particle-laden flow, Hypersonic flow, Dusty flow

1. INTRODUCTION

During Martian reentry, a major concern is often the adverse effects of dust particles suspended in the atmosphere on thermal protection systems. An overview of the interactions among the particles, the flow, and the vehicle is provided in Reference [1]. In particular, particles can collide with the heat shield, enhancing erosion [2] and augmenting surface heat fluxes via conversion of kinetic energy to heat. Furthermore, the strong nonequilibrium between the disperse and carrier phases in the shock layer causes significant momentum and energy transfer between the two phases (two-way-coupling). Particles can also accumulate near the surface and subsequently screen the surface from incoming particles, attenuating the heat flux augmentation [3]. The overall effect of the dust particles on the flow depends on the flow conditions, particle size, and particle mass loading.

In this paper, we present numerical simulations of high-speed dusty flows over blunt bodies with application to Mars atmospheric entry. In these simulations, the carrier gas is computed using the discontinuous Galerkin (DG) scheme, which is a finite-element-based method that borrows features from classical finite-volume schemes. In addition to high-order accuracy, DG methods can also account for surface curvature. It has also been shown that for certain hypersonic flows, DG predictions of stagnation heating are much less sensitive to grid-shock alignment and inviscid flux function than finite-volume predictions [4]. The disperse phase is calculated using a Lagrangian particle method that we developed under the DG framework [5]. The particle method includes two-way-coupling capabilities and is compatible with curved, high-aspect-ratio elements (often employed in DG simulations), specifically

in the context of particle-wall collisions. The use of curved elements can significantly improve prediction of particle trajectories. More recently, we have also developed an algorithm for handling interparticle collisions (four-way-coupling). This Euler-Lagrange framework is employed to compute representative test cases. Quantitative comparisons with experiments are provided, and the importance of accounting for interparticle collisions is assessed.

2. MATHEMATICAL FORMULATION

2.1. Governing equations of the carrier phase

The carrier gas is governed by the compressible Navier-Stokes equations, written in vector form as

$$\partial_t \mathbf{U} + \nabla \cdot \mathbf{F_i} = \nabla \cdot \mathbf{F_v} + \mathbf{S}, \tag{1}$$

where $\mathbf{U}(\boldsymbol{x}, t)$ is the conservative state vector, $\mathbf{F_i}(\mathbf{U})$ is the inviscid flux vector, $\mathbf{F_v}(\mathbf{U}, \nabla\mathbf{U})$ is the viscous flux vector, and $\mathbf{S}(\mathbf{U}, \nabla\mathbf{U})$ is the source term vector that accounts for the effect of the disperse phase on the carrier phase. The state vector can be expanded as $\mathbf{U} = [\rho, \rho\boldsymbol{u}, \rho E]^T$, where ρ is the density, $\boldsymbol{u}$ is the velocity vector, and E is the total energy per unit mass. To compute the dynamic viscosity, μ, we employ Sutherland's law. By the ideal gas law, the pressure, P, is related to internal energy as

$$P = (\gamma - 1)\left(\rho E - \frac{\rho}{2}|\boldsymbol{u}|^2\right). \tag{2}$$

2.2. Discontinuous Galerkin discretization

The problem is posed on the computational domain Ω with boundary $\partial\Omega$, with true solution $\mathbf{U}$. Ω is partitioned into N_e non-overlapping discrete elements such that $\Omega = \cup_{e=1}^{N_e}\Omega_e$. The boundary of element Ω_e is denoted by $\partial\Omega_e$. The local solution, $\mathbf{U}^e$, is approximated as

$$\mathbf{U}^e(\boldsymbol{x}, t) \approx \boldsymbol{U}^e(\boldsymbol{x}, t) = \sum_{n=1}^{N_b} \widetilde{\boldsymbol{U}}_n^e(t)\phi_n(\boldsymbol{x}), \tag{3}$$

where $\widetilde{\boldsymbol{U}}^e(t)$ are the N_b basis coefficients and ϕ_n is the nth basis function. In this work, we use a Lagrange polynomial basis.

The global solution approximation can then be written as

$$\boldsymbol{U} = \oplus_{e=1}^{N_e}\boldsymbol{U}^e. \tag{4}$$

To solve for the basis coefficients on Ω_e, we require $\widetilde{\boldsymbol{U}}^e(t)$ to satisfy

$$\sum_{n=1}^{N_b} d_t\widetilde{\boldsymbol{U}}_n^e(t)\int_{\Omega_e}\phi_m\phi_n d\Omega_e + \int_{\Omega_e}\phi_m\nabla\cdot\mathbf{F_i}d\Omega_e \tag{5}$$

$$= \int_{\Omega_e}\phi_m\nabla\cdot\mathbf{F_v}d\Omega_e + \int_{\Omega_e}\phi_m\mathbf{S}d\Omega_e\forall\ \phi_m. \tag{6}$$

In this study, we employ the Roe inviscid flux function [6] and the BR2 viscous flux function [7]. To evaluate integrals, we use standard Gaussian quadrature with an order of accuracy no less than $2p + 1$, where p is the user-prescribed order of the Lagrange polynomials.

2.3. Physical model of the disperse phase

The behavior of the disperse phase in the flow field is described via Lagrangian particle tracking. As is often done in particle-laden flow modeling, individual particles are treated as smooth, solid spheres. Particles are also assumed to be non-rotating, inert, and constant in size. It is assumed that the particle temperature is uniform over the entire particle. The particle state is computed using the following set of ordinary differential equations:

$$\frac{d\boldsymbol{x}_d}{dt} = \boldsymbol{u}_d, \tag{7a}$$

$$m_d\frac{d\boldsymbol{u}_d}{dt} = \boldsymbol{F} = \boldsymbol{F}_{qs} + \boldsymbol{F}_{\text{thermo}}, \tag{7b}$$

$$m_d c_d\frac{dT_d}{dt} = Q = \boldsymbol{Q}_{qs}, \tag{7c}$$

where the carrier and disperse phases are represented using the subscripts "c" and "d", respectively. $\boldsymbol{x}_d$ is the particle position, $\boldsymbol{u}_d$ is the particle velocity, $m_d = \rho_d\frac{\pi}{6}D^3$ is the particle mass (with ρ_d the particle density and D the particle diameter), c_d is the specific heat of the particle, and T_d is the particle temperature. The overall drag force, $\boldsymbol{F}$, is comprised of the quasi-steady drag and thermophoretic force, denoted $\boldsymbol{F}_{qs}$ and $\boldsymbol{F}_{\text{thermo}}$, respectively. The overall heating rate, Q, consists of quasi-steady heating, Q_{qs}. The quasi-steady contributions are given as

$$\boldsymbol{F}_{qs} = \frac{1}{8}\pi D^2\rho_c(\boldsymbol{u}_c - \boldsymbol{u}_d)|\boldsymbol{u}_c - \boldsymbol{u}_d|C_D, \tag{8a}$$

$$Q_{qs} = \pi D\kappa_c(T_c - T_d)\text{Nu}, \tag{8b}$$

where C_D is the drag coefficient, Nu is the Nusselt number, and κ_c is the thermal conductivity of the carrier gas. To compute C_D, we employ the Henderson drag correlation [8], and the Nusselt number correlation by Fox et al. is used to calculate Nu [9]. The Loth model is used to compute $\boldsymbol{F}_{\text{thermo}}$ [10]. In previous work, we investigated the importance of several other momentum and energy contributions and found that most of them are insignificant [11]. We also evaluated the influence of different drag and Nusselt number correlations and determined high sensitivity to the drag correlation. Our choice of drag and Nusselt number correlations is motivated by agreement with experiments as discussed in [5, 11].

2.4. Particle tracking methodology

The particle method is described in detail in Ref. [5]. It is briefly summarized here.

The source term vector $\mathbf{S} = [0, \boldsymbol{S}_m, S_e]^T$ on the RHS of Eq. (1) translates the effect of the disperse phase to the Eulerian flow field. We assume that there is no mass transfer. The momentum and energy contributions are given as

$$\boldsymbol{S}_m = -\sum_{i=1}^{N_p} \boldsymbol{F}_i \delta(\boldsymbol{x} - \boldsymbol{x}_{d,i}), \tag{9a}$$

$$S_e = -\sum_{i=1}^{N_p} \Big(Q_i + \boldsymbol{u}_{d,i} \cdot \boldsymbol{F}_i \Big) \delta(\boldsymbol{x} - \boldsymbol{x}_{d,i}), \tag{9b}$$

where $\delta(\boldsymbol{x} - \boldsymbol{x}_{d,i})$ is the Dirac delta function. With this choice of shape function, the source term in Eq. (5) can be evaluated for Ω_e analytically as

$$\int_{\Omega_e} \phi_m \boldsymbol{S} d\Omega_e = \sum_{i=1}^{N_p^e} \phi_m(\boldsymbol{x}_{d,i}) [0, \boldsymbol{F}_i, Q_i + \boldsymbol{u}_{d,i} \cdot \boldsymbol{F}_i]^T, \tag{10}$$

where N_p^e is the number of particles located in element Ω_e. This leads to a straightforward two-way-coupling methodology with subcell-varying source-term contributions.

To obtain $\boldsymbol{F}$ and Q in Eqs. (7), the state of the carrier phase must be interpolated to particle positions. This is natural under a discontinuous Galerkin framework since the carrier phase solution is already approximated using polynomials. As such, we use the same polynomials to obtain accurate interpolations anywhere in the computational domain. Doing so requires not only identifying the host element of each particle but also mapping the physical position of the particle to the reference position associated with the parent element. This can be difficult with unstructured grids with curved elements, which are often employed in DG simulations. A simplified variant of the algorithm by Allievi and Bermejo [12] is thus employed. This search-locate algorithm exploits information provided by the geometric mapping in order to efficiently identify the host cell of a given particle.

Another major challenge associated with curved, high-aspect-ratio elements is the treatment of particle-wall collisions. For conventional straight-sided elements, it is straightforward to determine intersections between the particle trajectory and wall boundary faces. However, in general for curved faces, this must be done iteratively. Thus, we employ a Newton search based on the geometric mapping from physical space to reference space. There also exist pathological cases not observed on straight-sided elements. Further details are provided in Ref. [5]. Despite the complexities of handling curved elements, such elements can also significantly improve prediction of particle trajectories in configurations with wall collisions.

A new feature of the particle method not discussed in Ref. [5] is treatment of particle-particle collisions. Given the computational overhead of dealing with interparticle collisions, most particle methods employ an algorithm to reduce the number of particle pairs to inspect for potential collisions. A frequently employed scheme is to compare a given particle with the particles in all vertex-sharing elements [13]. We propose an algorithm that can further decrease the number of particle pair inspections by leveraging information on particle locations provided by the geometric mapping from physical space to reference space. The algorithm has been verified by comparing with collision statistics given by kinetic theory.

3. RESULTS

3.1. Hypersonic dusty flow over a small sphere

In this test case, we investigate the experiments conducted by Vasilevskii et al. [14, 15] in the U1-1M shock tunnel at the Central Aerohydrodynamics Institute (CAHI). They considered dusty flows over aluminum spheres with a freestream Mach number of 6.1 using different dust materials, sizes, and concentrations.

Since Vasilevskii et al. report only the ratio between the dusty-gas heat flux and the pure-gas heat flux at the stagnation point, we focus here on the accurate prediction of dust-induced surface heat flux augmentation near the stagnation point.

In Ref. [5], we obtained good agreement with the experiments for a number of flow conditions. It was found that under the investigated conditions, collisional energy transfer at the surface was not significant. Instead, the dust-induced surface heat flux augmentation can be attributed to an increase in the shock layer temperature due to momentum and energy transfer with the flow field. Interparticle collisions were not taken into account. Here, we target two additional sets of flow conditions, described in Table 1, in which collisional energy transfer is more significant. We also evaluate the importance of accounting for particle-particle collisions under the conditions considered.

Table 1. Flow conditions for hypersonic dusty flow over a sphere. $P_{t,\infty}$ is the freestream total pressure, R_s is the radius of the aluminum sphere, β is the mass loading ratio, and $\overline{(\cdot)}$ denotes the averaging procedure described by Vasilevskii et al. [15]. For both cases, the freestream Mach number and total temperature are 6.1 and 570 K, respectively.

Case	$P_{t,\infty}$ (bar)	R_s (m)	Dust material	$\overline{D}$ (μm)	β (%)
1	7.8	0.012	SiO_2	0.19	1.8
2	17.5	0.006	Fe_2O_3	0.37	1.0

A hexahedral mesh with 60,000 elements is used to represent only the forebody of the sphere. We use curved (of quadratic order), high-aspect-ratio elements near the sphere surface to accurately capture the sharp temperature and density gradients as well as the curvature of the sphere. Freestream conditions are specified at the inflow boundary, interior quantities are extrapolated to the outflow boundary, and the sphere wall is an isothermal no-slip wall at $T = 300$ K. We use $p = 2$ polynomials to compute the DG solutions, yielding nominal third-order accuracy for smooth flows. There are no appreciable changes with $p = 3$ polynomials. We employ implicit third-order backward differencing and the third-order Adams-Bashforth method to integrate the carrier and disperse phases, respectively, in time. Particles are injected at each time step along the inflow boundary assuming equilibrium with the gas, i.e. the same velocity and temperature. The coefficients of restitution at the wall are computed using the correlations by Stasenko [16], based on surface material properties and particle incident velocity. All simulations are run until quasi-steady-state conditions are reached.

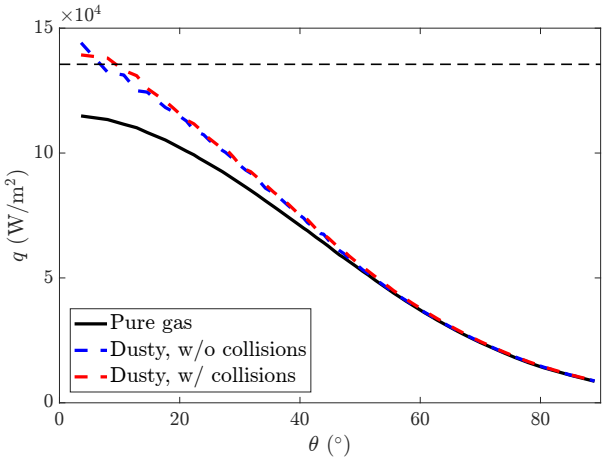

(a) Case 1 (SiO_2 particles, $P_{t,\infty}$ = 7.8 bar, R_s = 0.012 m, $\beta = 0.018$).

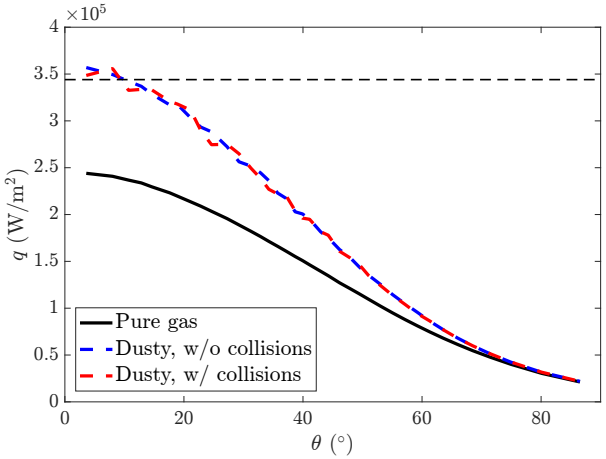

(b) Case 2 (Fe_2O_3 particles, $P_{t,\infty}$ = 17.5 bar, R_s = 0.006 m, $\beta = 0.01$).

Fig. 1. Pure-gas and dusty-gas surface heat flux profiles for the two cases listed in Table 1. The black dashed lines represent the stagnation-point heat flux obtained by scaling the experimental stagnation-point heat flux ratio [14, 15] by data from the pure-gas DG solutions. θ is the polar angle with respect to an axis pointing from the center of the sphere to the stagnation point. Results for computations with and without particle-particle collisions are included.

Figure 1 displays the pure-gas and dusty-gas heat flux profiles (averaged azimuthally and temporally) for the two sets of flow conditions described in Table 1. The black dashed lines represent the stagnation-point heat flux obtained by scaling the experimental stagnation-point heat flux ratio [14, 15] by data from the pure-gas DG solutions. In both cases, although there is slight overprediction of the stagnation-point heat flux, good overall agreement is observed. In Case 2 (Figure 1(b)), the stagnation-point heat flux increases by over 40%, which is much greater than in Case 1 (Figure 1(a)). Despite a lower mass loading, the bigger particles in Case 2 retain more of their initial speed while traversing the shock layer and transfer more kinetic energy to the sphere upon collision. Conversely, in Case 1, the smaller particles lose more of their momentum to the carrier gas and hit the sphere at lower speeds. In both cases, the effect of particle-particle collisions is small. Different flow conditions, such as higher particle concentrations and speeds, would likely increase the effect of accounting for interparticle collisions. This will be further discussed in Section 3.2.

3.2. High-speed dusty flow over a reentry capsule at Mars atmospheric conditions

In this section, we investigate a more realistic flow configuration of supersonic/hypersonic dusty flow over a reentry capsule forebody. We target three trajectory points from the ExoMars Schiaparelli entry mission [17], detailed in Table 2. The freestream Mach numbers range from 3.55 to 8.97. For simplicity, the angle of attack is set to zero. The capsule diameter is 3.91 m. CO_2 is used as the working gas. Of primary interest is the effect of interparticle collisions on heat flux augmentation at the conditions considered.

Table 2. Freestream gas conditions for high-speed dusty flow over a reentry capsule, taken from the trajectory of the ExoMars Schiaparelli vehicle [17].

Trajectory point	Mach	$\rho \times 10^3$ (kg/m^3)	P (Pa)	T (K)
S3	8.97	1.98	74.1	195
S5	5.43	2.96	114	202
S7	3.55	4.08	164	210

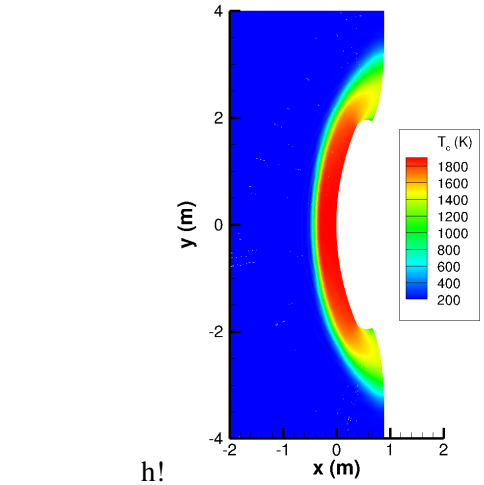

h!

(a) S3 (Ma = 8.97)

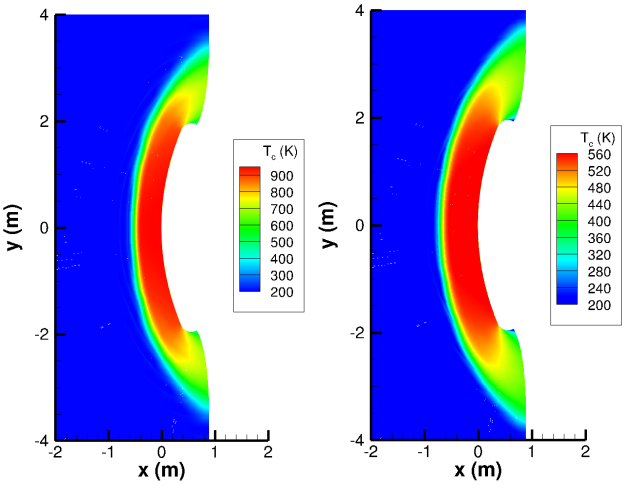

(b) S5 (Ma = 5.43) (c) S7 (Ma = 3.55)

Fig. 2. Pure-gas temperature fields for supersonic/hypersonic flows over a reentry capsule with flow conditions defined in Table 2.

As is commonly done in simulations involving Mars atmospheric dust, SiO_2 is chosen to represent the dust material [18]. For particle size, we employ the modified gamma distribution by Tomasko et al. [19], which gives a geometric cross-section-weighted mean particle radius of 1.6 μm. The dust mass loading ratio is set to 2.4%, which, for the S5 trajectory point, corresponds to the bulk density of 7×10^{-5} kg/m^3 reported by Metzger et al. [20] for a dust storm.

The setup of the carrier gas solution is similar to that in Section 3.1. We use a hexahedral mesh with 55,000 elements and $p = 2$ polynomials, with nominal third-order accuracy in smooth regions. Particles are injected

at freestream gas conditions at each time step along a cut plane upstream of the shock. The correlations by Stasenko [16] are again employed to calculate coefficients of restitution for wall collisions. We consider the capsule material to be the same as that of the Schiaparelli heat shield, Norcoat-Liège [21]. Simulations are run until a quasi-steady-state is reached. Given the significantly larger size of the particles than in Section 3.1 as well as the strong nonequilibrium between the two phases in the shock layer, especially for the S3 trajectory point, the back-coupling of particles to the carrier gas is ignored in order to avoid instabilities. Smooth shape functions, as opposed to the delta functions discussed in Section 2.4, would alleviate this issue, which will be the subject of future work. Nevertheless, for the higher freestream Mach numbers, collisional energy transfer at the surface is expected to dominate, and since we aim to assess the importance of interparticle collisions, similar qualitative conclusions can likely be drawn.

The pure-gas temperature fields for the three trajectory points are displayed in Figure 2. In all cases, the bow shock is smoothly captured and free from apparent oscillations. The temperature jump in the S3 case is much greater than in the S5 and S7 cases, and the shock is closer to the capsule.

Figure 3 shows the dusty-gas and pure-gas heat flux profiles, averaged azimuthally and temporally. For the S7 trajectory point, there is almost no heat flux augmentation. Particles are initialized at much lower velocities, and due to the thicker shock layer, there is a longer residence time for particles to equilibrate with the carrier gas. Therefore, most particles are simply advected past the vehicle without reaching the surface, and the particles that do hit the capsule transfer very little energy. With hardly any heating augmentation, there is almost no difference between the computations with and without interparticle collisions. For the S5 trajectory point, there is noticeable heat flux augmentation due to the higher initial velocities and thinner shock layer. As a result, many particles collide with the surface with appreciable kinetic energy. When taking into account interparticle collisions, there is slight heat flux attenuation, which is evidence of the screening effect discussed in Section 1, but the overall effect is quite small.

Heat flux augmentation is greatest in the S3 case. Particles retain much of their kinetic energy and hit the surface at high velocities. Based on the coefficients of restitution obtained from the correlations by Stasenko

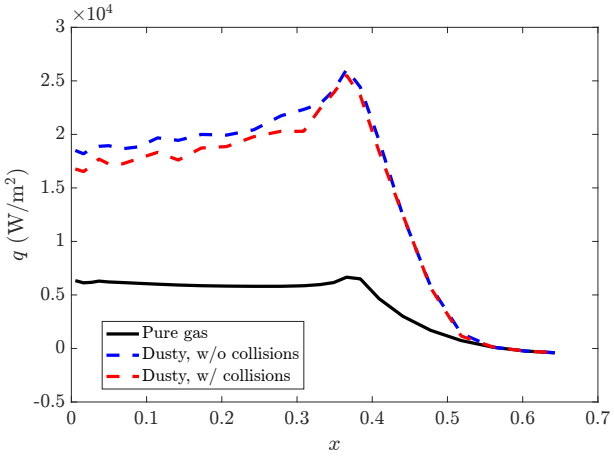

(a) S3 (Ma = 8.97)

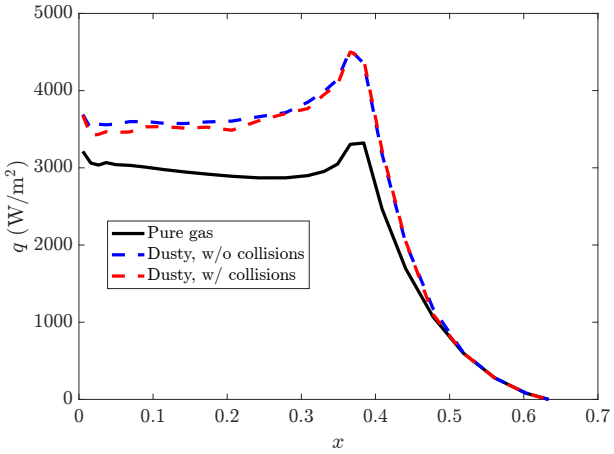

(b) S5 (Ma = 5.43)

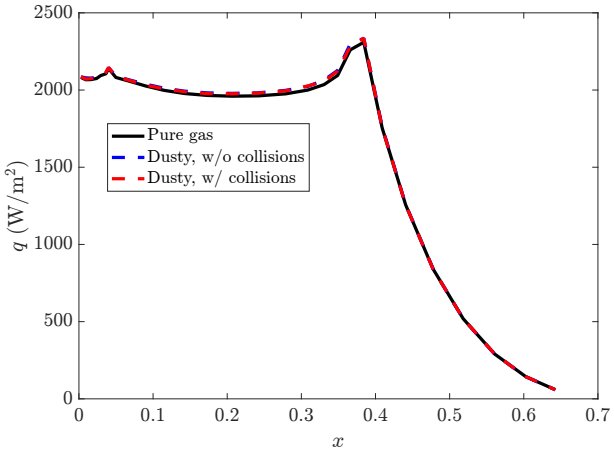

(c) S7 (Ma = 3.55)

Fig. 3. Pure-gas and dusty-gas heat flux profiles for supersonic/hypersonic flows over a reentry capsule with flow conditions defined in Table 2. Results for computations with and without particle-particle collisions are included. x is the streamwise direction.

[16], the particles are reflected at low velocities and accumulate near the surface of the vehicle. Combined with the significant incoming kinetic energy flux of the particles, this gives rise to the most apparent screening out of all three cases. There is appreciable heat flux attenuation up to the aft corner of the capsule as a result of this screening effect. For the higher Mach numbers at earlier points in the trajectory, the effect of these collisions would likely increase.

The results of these simulations demonstrate that higher Mach numbers lead to greater collisional energy transfer. At the same time, the magnitude of heat flux attenuation also increases with Mach number. The amount of heat flux augmentation and attenuation from interparticle collisions depends on other factors too. For example, a higher mass loading would similarly cause greater collisional energy transfer and heating attenuation. The bluntness of the capsule, compared to the sphere in Section 3.1, likely enhances the number of particle-wall and particle-particle collisions.

4. CONCLUDING REMARKS

Dust-induced heat flux augmentation in high-speed dusty flows over blunt bodies is numerically investigated. This is relevant to Mars reentry missions since the high concentration of dust particles suspended in the Mars atmosphere can collide with vehicles and modify the flow field via momentum and energy transfer. We employ an Euler-Lagrange methodology in which the carrier gas solution is obtained with the DG method, which offers high-order accuracy and insensitivity to mesh topology and flux functions, while the disperse phase is treated with Lagrangian particle tracking.

The first test case consists of hypersonic dusty flow over a small aluminum sphere. Experiments were performed by Vasilevskii et al. [14, 15]. Two sets of flow conditions, one with SiO_2 and the other with Fe_2O_3 particles, are investigated. The larger Fe_2O_3 particles yield greater heat flux augmentation since they transfer less momentum and energy to the carrier gas than the smaller SiO_2 particles and they collide with the sphere at higher speeds. Despite slight overprediction, good agreement with the experimental results is observed. Under the flow conditions considered, the effect of interparticle collisions is not significant.

In the second test case, we investigate a more realistic flow configuration. Instead of a sphere, we use a reentry capsule. We also target three trajectory points from the ExoMars Schiaparelli entry mission, and we employ a particle size distribution and mass loading reported in the literature for suspended Martian dust. The magnitude of collisional energy transfer increases with Mach number since particle initial velocities are higher and there is less time for particles to transfer their momentum to the carrier gas. The effect of interparticle collisions also increases with Mach number. At the highest Mach number, particles hit the vehicle surface at high velocities and are reflected with low velocities. These particles accumulate and then shield the vehicle from the subsequent incoming particle energy flux.

Future work will involve the development of smooth shape functions, instead of delta functions, for the back-coupling of particles to the Eulerian field. This will help avoid instabilities and allow for consideration of two-way-coupling when simulating hypersonic dusty flow over a reentry vehicle at realistic Mars atmospheric and dust conditions. We will also simulate the aftbody and assess how particles will affect the flow field and surface heating in this region. We also plan to further investigate sensitivities to various components and parameters in the dusty flow model, such as dust loading, particle properties, vehicle shape and size, etc. Other effects of the dust particles, such as erosion, may also be investigated. Finally, we will extend the DG solver to higher temperatures, where thermal nonequilibrium and ionization/dissociation chemistry can become significant.

5. REFERENCES

[1] I. Montois, D. Pirotais, D. Conte, N. Sauvage, and O. Chazot, "Overview of dust effects during mars atmospheric entries: Models, facilities, and design tools," Tech. Rep., Pasadena, CA, 2007.

[2] G. Palmer, Y.-K. Chen, P. Papadopoulos, and M. Tauber, "Reassessment of effect of dust erosion on heatshield of Mars entry vehicle," *J. Spacecraft Rockets*, vol. 37, no. 4, 2000.

[3] A. N. Volkov and Y. M. Tsirkunov, "Effect of a dispersed admixture on the flow pattern and heat transfer in a supersonic dusty-gas flow around a cylinder," *Fluid Dynamics*, vol. 40, no. 4, pp. 561–574, 2005.

[4] E. J. Ching, Y. Lv, P. Gnoffo, M. Barnhardt, and

M. Ihme, "Shock capturing for discontinuous Galerkin methods with application to predicting heat transfer in hypersonic flows," *Journal of Computational Physics*, vol. 376, pp. 54–75, 2019.

[5] E. J. Ching, S. R. Brill, Y. Lv, M. D. Barnhardt, and M. Ihme, "An Euler-Lagrange method for simulating high-speed multiphase flows with two-way-coupling using discontinuous Galerkin schemes on arbitrary curved elements," submitted, 2019.

[6] P. L. Roe, "Approximate Riemann solvers, parameter vectors, and difference schemes," *Journal of Computational Physics*, vol. 43, no. 2, pp. 357–372, 1981.

[7] F. Bassi and S. Rebay, "GMRES discontinuous Galerkin solution of the compressible Navier-Stokes equations," in *Discontinuous Galerkin Methods: Theory, Computation and Applications*, B. Cockburn and C. W. Shu, Eds., pp. 197–208. Springer, Berlin, 2000.

[8] Charles B Henderson, "Drag coefficients of spheres in continuum and rarefied flows," *AIAA Journal*, vol. 14, no. 6, pp. 707–708, 1976.

[9] T. W. Fox, C. W. Rackett, and J. A. Nicholls, "Shock wave ignition of magnesium powers," in *11th International Shock Tubes and Waves Symposium*, Seattle, Washington, 1978, pp. 262–268.

[10] E. Loth, "Compressibility and rarefaction effects on drag of a spherical particle," *AIAA Journal*, vol. 46, no. 9, pp. 2219–2228, 2008.

[11] E. J. Ching and M. Ihme, "Sensitivity study of high-speed dusty flows over blunt bodies simulated using a discontinuous Galerkin method," in *AIAA Scitech 2019 Forum*, 2019, p. 0895.

[12] A. Allievi and R. Bermejo, "A generalized particle search-locate algorithm for arbitrary grids," *Journal of Computational Physics*, vol. 132, pp. 157–166, 1997.

[13] S. Sundaram and L. R. Collins, "Numerical considerations in simulating a turbulent suspension of finite-volume particles," *Journal of Computational Physics*, vol. 124, no. 2, pp. 337–350, 1996.

[14] E. Vasilevskii and A. Osiptsov, "Experimental and numerical study of heat transfer on a blunt body in dusty hypersonic flow," in *33rd AIAA Thermophysics Conference*, Norfolk, Virginia, 1999, AIAA 1999-3563.

[15] E. B. Vasilevskii, A. N. Osiptsov, A. V. Chirikhin, and L. V. Yakovleva, "Heat exchange on the front surface of a blunt body in a high-speed flow containing low-inertia particles," *Journal of Engineering Physics and Thermophysics*, vol. 74, no. 6, pp. 1399–1411, 2001.

[16] A. L. Stasenko, "Velocity recovery factors of a particle repelled from a solid surface," *Journal of Engineering Physics and Thermophysics*, vol. 80, no. 5, pp. 885–891, 2007.

[17] A. Gülhan, T. Thiele, F. Siebe, R. Kronen, and T. Schleutker, "Aerothermal measurements from the ExoMars Schiaparelli capsule entry," *Journal of Spacecraft and Rockets*, vol. 56, no. 1, pp. 68–81, 2018.

[18] T. Ozawa, T. Suzuki, H. Takayanagi, and K. Fujita, "Investigation of Martian-dust drag and heat transfer for Mars sample return mission," *Journal of Thermophysics and Heat Transfer*, vol. 25, no. 3, pp. 341–353, 2011.

[19] M. G. Tomasko, L. R. Doose, M. Lemmon, P. H. Smith, and E. Wegryn, "Properties of dust in the Martian atmosphere from the Imager on Mars Pathfinder," *Journal of Geophysical Research: Planets*, vol. 104, no. E4, pp. 8987–9007, 1999.

[20] S. M. Metzger, J. R. Carr, J. R. Johnson, T. J. Parker, and M. T. Lemmon, "Dust devil vortices seen by the Mars Pathfinder camera," *Geophysical Research Letters*, vol. 26, no. 18, pp. 2781–2784, 1999.

[21] S. Portigliotti, C. Cassi, M. Montagna, P. Martella, M. Faletra, J. Boi, S. De Sanctis, D. Granà, O. Bayle, T. Blancquaert, et al., "ExoMars 2016, the Schiaparelli mission. EDL demonstration results from real time telemetry before unfortunate impact," in *14th International Planetary Probe Workshop*, 2017.